JOURNAL OF COMPUTATIONAL PHYSICS 121, 66–78 (1995)

Accurate Flux Vector Splitting for Shocks and Shear Layers

R. RADESPIEL AND N. KROLL

DLR, Institute of Design Aerodynamics, Braunschweig, Germany

Received February 15, 1994; revised March 6, 1995

The advection upstream splitting method (AUSM) was recently developed by Liou and Steffen for accurate predictions of viscous flows. The special merits of AUSM compared to other upwind schemes are the low computational complexity and the low numerical diffusion. However, it is known that the original method also has several deficiencies. It locally produces pressure oscillations in the vicinity of shocks and in cases of adverse grid situations and flow alignment. In this paper a hybrid flux vector splitting scheme is proposed which switches from AUSM to van Leer at shock waves, ensuring a sharp and clean resolution of strong shocks. In order to achieve sufficient damping, a modified dissipative term is introduced, which prevents the scheme from being undamped as the Mach number approaches zero. Various modifications of the standard MUSCL implementations for second-order accuracy are proposed, which yield an accurate resolution of viscous shear layers without spurious oscillations. The ability of the improved flux vector splitting scheme is demonstrated by the computation of two- and three-dimensional viscous flows. © 1995 Academic Press, Inc.

1. INTRODUCTION

The prediction of the extreme flow conditions found in high-speed flows requires accurate and robust numerical methods. This has led to the development of the so-called upwind-biased discretization schemes. In contrast to central difference approximations these methods use local wave propagation theory to produce accurate evaluations of flow properties near discontinuities and shear layers without the necessity of added artificial damping. However, in comparison with central discretization these methods require higher computational effort.

In the past, several upwind schemes have been developed and successfully used for the calculation of many inviscid flow problems. Prominent representatives of this class of algorithms are schemes based on the *flux vector splitting* (e.g. [1, 2]) and *flux difference splitting* (e.g., [3, 4]) concepts. Investigations have shown that when used for viscous flow calculations most of these schemes turn out to be either inaccurate or difficult to use with respect to robustness and parameter sensitivity. Classical flux vector splitting methods are simple and very robust upwind techniques but they exaggerate diffusive effects which take place in shear and boundary layers. On the other hand, schemes based on flux difference splitting are very accurate for viscous calculations, but at the cost of increased computational expense. Moreover, they lack robustness for flows with strong expansions into regions of low pressure and low density.

Consequently, substantial effort has been put on the development of modified or new upwind methods (e.g., [5–7]) with the primary goal of maximizing both accuracy and computational efficiency. A remarkably simple upwind flux vector splitting scheme has been introduced by Liou and Steffen [6, 8]. It treats the convective and pressure terms of the flux function separately. The convective quantities are upwind-biased extrapolated to the cell interface using a properly defined cell face advection Mach number. Accordingly, the scheme is called *advection upstream splitting method* (AUSM). Results for simple flow problems given by Liou [6, 8] have shown that AUSM retains the robustness and efficiency of the flux vector splitting schemes but it achieves the high accuracy attributed to schemes based on the flux difference splitting concept. The computational effort for the flux evaluation is only linearly proportional to the number of unknowns, as in the case of central differencing. Furthermore, the scheme can be easily extended to real gas calculations. The application to various relevant flow problems, however, has shown [9–10] that the original flux vector splitting method of Liou and Steffen has several deficiencies. It locally produces pressure oscillations in the vicinity of shocks. Furthermore, the scheme has a poor damping behavior for low Mach numbers which leads to spurious oscillations in the solution and affects the ability of the scheme to capture flows aligned with the coordinate grids.

In the present paper several modifications to the original advection upstream splitting method of Liou and Steffen are proposed which substantially improve the scheme's ability to predict viscous flows accurately. In particular, a hybrid method is introduced which switches from AUSM to the van Leer scheme at shock waves. This ensures the well-known sharp and clean shock capturing capability of the van Leer scheme and the high resolution of slip lines and contact discontinuities through AUSM. An adaptive dissipation is introduced in order to achieve sufficient numerical damping in cases of adverse grid situations and flow alignment. Furthermore, the MUSCL implementation for higher order accuracy is modified to allow

0021-9991/95 $12.00
Copyright © 1995 by Academic Press, Inc.
All rights of reproduction in any form reserved.

a more accurate scaling of the numerical dissipation in boundary layers where the contravariant Mach number is usually small in the wall-normal direction. The improved accuracy of the modified scheme is demonstrated by the calculation of two- and three-dimensional inviscid and viscous flows.

2. GOVERNING EQUATIONS

The integral form of the three-dimensional mass-averaged Navier–Stokes equations using nondimensional variables in a cartesian coordinate system can be written as

$$\frac{\partial}{\partial t}\int_V \mathbf{W}\, dV + \int_{\partial V} \overline{F}\cdot\mathbf{n}\, ds = 0, \tag{1}$$

where

$$\mathbf{W} = [\rho, \rho u, \rho v, \rho w, \rho E]^T$$

is the vector of conserved quantities with ρ, u, v, w, and E, denoting the density, cartesian velocity components, and specific total energy, respectively. V denotes an arbitrary control olume fixed in time and space with boundary ∂V and the outer normal $\mathbf{n}$. The total enthalpy is given by

$$H = E + p/\rho. \tag{2}$$

The flux tensor $\overline{F}$ may be divided into its inviscid part $\overline{F}^I$ and its viscous part $\overline{F}^v$ as

$$\overline{F} = \overline{F}^I - \overline{F}^v \tag{3}$$

with

$$\overline{F}^I = \begin{bmatrix} \rho u\mathbf{k}_x & + \rho v\mathbf{k}_y & + \rho w\mathbf{k}_z \\ (\rho u^2 + p)\mathbf{k}_x & + \rho uv\mathbf{k}_y & + \rho uw\mathbf{k}_z \\ (\rho uv)\mathbf{k}_x & + (\rho v^2 + p)\mathbf{k}_y & + \rho vw\mathbf{k}_z \\ (\rho uw)\mathbf{k}_x & + \rho vw\mathbf{k}_y & + (\rho w^2 + p)\mathbf{k}_z \\ (\rho uE + up)\mathbf{k}_x & + (\rho vE + vp)\mathbf{k}_y & + (\rho wE + wp)\mathbf{k}_z \end{bmatrix}$$

and

$$\overline{F}^v = \begin{bmatrix} 0 & & \\ \sigma_{xx}\mathbf{k}_x & + \sigma_{xy}\mathbf{k}_y & + \sigma_{xz}\mathbf{k}_z \\ \sigma_{yx}\mathbf{k}_x & + \sigma_{yy}\mathbf{k}_y & + \sigma_{yz}\mathbf{k}_z \\ \sigma_{zx}\mathbf{k}_x & + \sigma_{zy}\mathbf{k}_y & + \sigma_{zz}\mathbf{k}_z \\ (u\sigma_{xx} + v\sigma_{xy} + w\sigma_{xz} - q_x)\mathbf{k}_x & + (u\sigma_{yx} + v\sigma_{yy} + w\sigma_{yz} - q_y)\mathbf{k}_y & + (u\sigma_{zx} + v\sigma_{zy} + w\sigma_{zz} - q_z)\mathbf{k}_z \end{bmatrix},$$

where $\mathbf{k}_x$, $\mathbf{k}_y$, $\mathbf{k}_z$ denote the cartesian coordinate directions. Assuming that air behaves as a calorically perfect gas, the pressure is calculated by the equation of state

$$p = (\gamma - 1)\rho\left(E - \frac{u^2 + v^2 + w^2}{2}\right), \tag{4}$$

where γ denotes the ratio of specific heats. The temperature T is given by

$$T = p/\rho. \tag{5}$$

The elements of the shear–stress tensor and the heat–flux vector are given by the equations for Newtonian fluid

$$\begin{aligned} \sigma_{xx} &= 2\mu u_x - 2/3\mu(u_x + v_y + w_z) \\ \sigma_{yy} &= 2\mu v_y - 2/3\mu(u_x + v_y + w_z) \\ \sigma_{zz} &= 2\mu w_z - 2/3\mu(u_x + v_y + w_z) \\ \sigma_{xy} &= \sigma_{yx} = \mu(u_y + v_x) \\ \sigma_{xz} &= \sigma_{zx} = \mu(u_z + w_x) \\ \sigma_{yz} &= \sigma_{zy} = \mu(v_z + w_y) \\ q_x &= -K\frac{\partial T}{\partial X}, \quad q_y = -K\frac{\partial T}{\partial y}, \quad q_z = -K\frac{\partial T}{\partial z}. \end{aligned} \tag{6}$$

For laminar flow the nondimensional viscosity μ is assumed to follow the Sutherland law

$$\mu = \frac{\gamma^{1/2}\mathrm{M}_\infty}{\mathrm{Re}_\infty}\left(\frac{\overline{T}}{\overline{T}_\infty}\right)^{3/2}\frac{\overline{T}_\infty + 110k}{\overline{T} + 110k} \tag{7}$$

with M_∞, Re_∞, and $\overline{T}$ denoting the free stream Mach number, Reynolds number, and the dimensional temperature, respectively. The heat conductivity K is given by

$$K = \frac{\gamma}{\gamma - 1}\frac{\mu}{\mathrm{Pr}} \tag{8}$$

with Pr being the Prandtl number.

For turbulent flows, the laminar viscosity μ in Eq. (7) is replaced by $\mu + \mu_t$ and μ/Pr in Eq. (8) is replaced by $\mu/\mathrm{Pr} + \mu_t/\mathrm{Pr}_t$, where the eddy viscosity μ_t and the turbulent Prandtl Pr_t number are provided by a turbulence model. For the transonic airfoil calculations presented in this paper the algebraic turbulence model of Baldwin and Lomax [11] is used.

For hypersonic flow calculations it is assumed that air be-

haves as air reacting in thermochemical equilibrium. In this case a modified ratio of specific heats is used. Furthermore, the speed of sound is given by

$$c^2 = \left.\frac{\partial p}{\partial \rho}\right|_{e=\text{const}} + \frac{p}{\rho}\left.\frac{\partial p}{\partial e}\right|_{\rho=\text{const}}, \tag{9}$$

where e is the internal energy per unit mass. For the calculation of the effective ratio of specific heats and for the partial derivatives of pressure in Eq. (9), piecewise analytically defined functions [12] are used. These functions relate the pressure to both the density and specific internal energy and take into account the exitation of vibration and the dissociation of O_2 and N_2 molecules. The temperature, viscosity, and heat conductivity are similarly computed.

3. SOLUTION METHOD

3.1. *First-Order Spatial Discretization*

The numerical method is based on a finite volume discretization. The approximation of the governing equations (1) follows the method of lines which decouples the discretization in space and time. The generation of a body-fitted grid around the aerodynamic body under investigation divides the physical domain into hexahedral cells. The discrete values of the flow quantities are located at the vertices of the mesh cells. For the flux calculation an auxiliary grid is used which is defined by connecting the cell centers of the original mesh. The approximation of the integral equation (1) for a hexahedral control volume surrounding the grid node (i, j, k) yields a system of ordinary differential equations with respect to time,

$$V_{i,j,k} \cdot \frac{\partial}{\partial t}\mathbf{W}_{i,j,k} = -\mathbf{R}_{i,j,k}. \tag{10}$$

$\mathbf{R}_{i,j,k}$ represents the net flux (residuum) of mass, momentum, and energy over the control volume (i, j, k) with volume $V_{i,j,k}$. It is calculated as

$$\begin{aligned}\mathbf{R}_{i,j,k} = {} & \mathbf{R}_{i+1/2,j,k} - \mathbf{R}_{i-1/2,j,k} + \mathbf{R}_{i,j+1/2,k} \\ & - \mathbf{R}_{i,j-1/2,k} + \mathbf{R}_{i,j,k+1/2} - \mathbf{R}_{i,j,k-1/2},\end{aligned} \tag{11}$$

with

$$\mathbf{R}_{i+1/2,j,k} = \mathbf{R}^I_{i+1/2,j,k} - \mathbf{R}^V_{i+1/2,j,k}, \tag{12}$$

where $\mathbf{R}^I_{i+1/2,j,k}$ and $\mathbf{R}^V_{i+1/2,j,k}$ denote the inviscid and viscous flux through cell face $i + 1/2$.

In the following the improved flux vector splitting scheme is described. Here, only the approximation of the convective flux is discussed. Viscous fluxes are taken into account only in the coordinate direction normal to the body surface (thin layer approximation of the Navier–Stokes equations). As usual, they are discretized with central differences. Details of the viscous flux approximation are given in [13].

As shown in [6], the discrete inviscid flux calculated by AUSM can be interpreted as a sum of a Mach number weighted average of the left (L) and right (R) state at the cell face $i + \frac{1}{2}$ between points (i, j, k) and $(i + 1, j, k)$ and a scalar dissipative term. It reads

$$\begin{aligned}\mathbf{R}_{i+1/2,j,k} = {} & |\mathbf{S}|_{i+1/2,j,k}\left(\frac{1}{2}M_{i+1/2,j,k}\left(\begin{bmatrix}\rho c\\ \rho cu\\ \rho cv\\ \rho cw\\ \rho cH\end{bmatrix}_L + \begin{bmatrix}\rho c\\ \rho cu\\ \rho cv\\ \rho cw\\ \rho cH\end{bmatrix}_R\right)\right. \\ & \left. - \frac{1}{2}\Phi_{i+1/2,j,k}\left(\begin{bmatrix}\rho c\\ \rho cu\\ \rho cv\\ \rho cw\\ \rho cH\end{bmatrix}_R - \begin{bmatrix}\rho c\\ \rho cu\\ \rho cv\\ \rho cw\\ \rho cH\end{bmatrix}_L\right)\right) + \begin{bmatrix}0\\ s_x p\\ s_y p\\ s_z p\\ 0\end{bmatrix}_{i+1/2,j,k},\end{aligned} \tag{13}$$

where

$$\mathbf{S}_{i+1/2,j,k} = [s_x, s_y, s_z]^T_{i+1/2,j,k} \tag{14}$$

denotes the surface vector normal to the cell face $i + \frac{1}{2}$. The quantity c represents the speed of sound. $M_{i+1/2,j,k}$ denotes the advection Mach number at the cell face $i + \frac{1}{2}$ which is calculated according to [6] as

$$M_{i+1/2,j,k} = \mathrm{M}^p_L + \mathrm{M}^m_R, \tag{15}$$

where the split Mach numbers $\mathrm{M}^{p/m}$ are defined following van Leer [2]:

$$\begin{aligned}\mathrm{M}^p &= \begin{cases}\mathrm{M}, & \text{if } \mathrm{M} \geq 1,\\ \frac{1}{4}(\mathrm{M}+1)^2, & \text{if } |\mathrm{M}| < 1,\\ 0, & \text{if } \mathrm{M} \leq -1;\end{cases}\\ \mathrm{M}^m &= \begin{cases}0, & \text{if } \mathrm{M} \geq 1,\\ -\frac{1}{4}(\mathrm{M}-1)^2, & \text{if } |\mathrm{M}| < 1,\\ \mathrm{M}, & \text{if } \mathrm{M} \leq -1.\end{cases}\end{aligned} \tag{16}$$

M_L and M_R denote the Mach number associated with the left and right state, respectively. The advection Mach number is given by

$$M = \frac{1}{|S|}\frac{(s_x u + s_y v + s_z w)}{c}. \tag{17}$$

The pressure p at cell face $i + \frac{1}{2}$ is calculated in a similar way

$$p_{i+1/2,j,k} = p_L^p + p_R^m, \tag{18}$$

where $p^{p/m}$ denote the split pressure defined according to [2]

$$p^p = \begin{cases} p, & \text{if } M \geq 1, \\ \frac{1}{4}p\,(M+1)^2(2-M), & \text{if } |M| < 1, \\ 0, & \text{if } M \leq -1; \end{cases}$$
$$p^m = \begin{cases} 0, & \text{if } M \geq 1, \\ \frac{1}{4}p(M-1)^2(2+M), & \text{if } |M| < 1, \\ p, & \text{if } M \leq -1. \end{cases} \tag{19}$$

The definition of the dissipative term Φ determines the particular formulation of the convective fluxes. A hybrid scheme is proposed here, which combines the van Leer scheme and the scheme of Liou and Steffen (AUSM). It reads

$$\phi_{i+1/2,j,k} = (1-\omega)\cdot\phi^{VL}_{i+1/2,j,k} + \omega\cdot\phi^{modAUSM}_{i+1/2,j,k} \tag{20}$$

with

$$\phi^{VL}_{i+1/2,j,k} = \begin{cases} |M_{i+1/2,j,k}|, & \text{if } |M_{i+1/2,j,k}| \geq 1, \\ |M_{i+1/2,j,k}| + \frac{1}{2}(M_R - 1)^2, & \text{if } 0 \leq M_{i+1/2,j,k} < 1, \\ |M_{i+1/2,j,k}| + \frac{1}{2}(M_L + 1)^2, & \text{if } -1 < M_{i+\frac{1}{2},j,k} \leq 0; \end{cases} \tag{21}$$

$$\phi^{modAUSM}_{i+1/2,j,k} = \begin{cases} |M_{i+1/2,j,k}|, & \text{if } |M_{i+1/2,j,k}| > \tilde{\delta}, \\ \dfrac{(M_{i+1/2,j,k})^2 + \tilde{\delta}^2}{2\tilde{\delta}}, & \text{if } |M_{i+1/2,j,k}| \leq \tilde{\delta}; \end{cases} \tag{22}$$

where $\tilde{\delta}$ is a small parameter, $0 < \tilde{\delta} \leq 0.5$, and ω is a constant, $0 \leq \omega \leq 1$.

The above equations clearly show that for a supersonic cell face Mach number the hybrid scheme represents a pure upwind discretization, using either the left or right state for the convective and pressure terms, depending on the sign of the Mach number. For $\omega = 0$ the method reduces to the classical van Leer flux vector splitting scheme. In the case of $\omega = 1$ and $\tilde{\delta} = 0$ the original AUSM developed by Liou and Steffen is recovered. Comparing both fluxes it is obvious that the van Leer scheme is more dissipative than AUSM ($\tilde{\delta} = 0$). It has

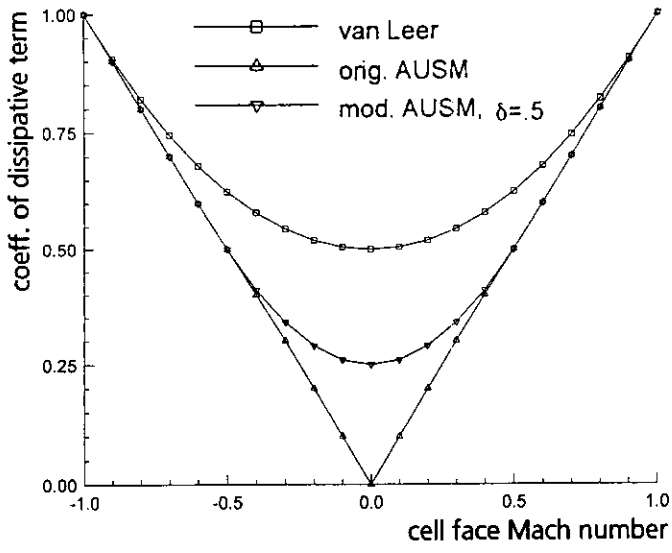

FIG. 1. Dissipation coefficient for Mach number close to zero.

an additional Mach number scaled dissipative term which does not vanish even for $M = 0$. Consequently, the van Leer scheme is more robust but less accurate than the original scheme of Liou and Steffen, especially for viscous flow calculations. It is interesting to note that the Mach number scaled dissipation of the advected flux fulfills the requirements for preconditioning the discrete flow equations given by Turkel [14]. Turkel proposes that the numerical dissipation should scale according to the eigenvalues of the preconditioned differential form of the flow equation, i.e., the convective wave speeds. Both the dissipation inherent in the split pressure, Eq. (19) and the advected part of the flux vector, Eq. (22) with $\tilde{\delta} = 0$, vanish as the contravariant velocity component goes to zero. In contrast, van Leer's dissipation scale, Φ^{VL}, is 0.5 for $M \to 0$. Hence, van Leer's dissipation scales with the acoustic wave speed for low Mach numbers where the speed of sound is approximately constant. This behavior is responsible for the failure of preconditioning, in combination with Van Leer's flux vector splitting as observed in [15].

The hybrid flux has been introduced in order to ensure both the clean and sharp shock resolution of the van Leer scheme and the low diffusive solution of the AUSM in smooth regions. This is realized by relating the parameter ω to the second difference of the pressure,

$$\omega = \max(\nu_{i,j,k}\nu_{i+1,j,k}),$$

$$\nu_{i,j,k} = \max\left(1 - \alpha\left|\frac{p_{i-1,j,k} - 2p_{i,j,k} + p_{i+1,j,k}}{p_{i-1,j,k} + 2p_{i,j,k} + p_{i+1,j,k}}\right|, 0\right), \quad \alpha = O(5). \tag{23}$$

The value of ω is 1 in smooth regions and switches to 0 in the

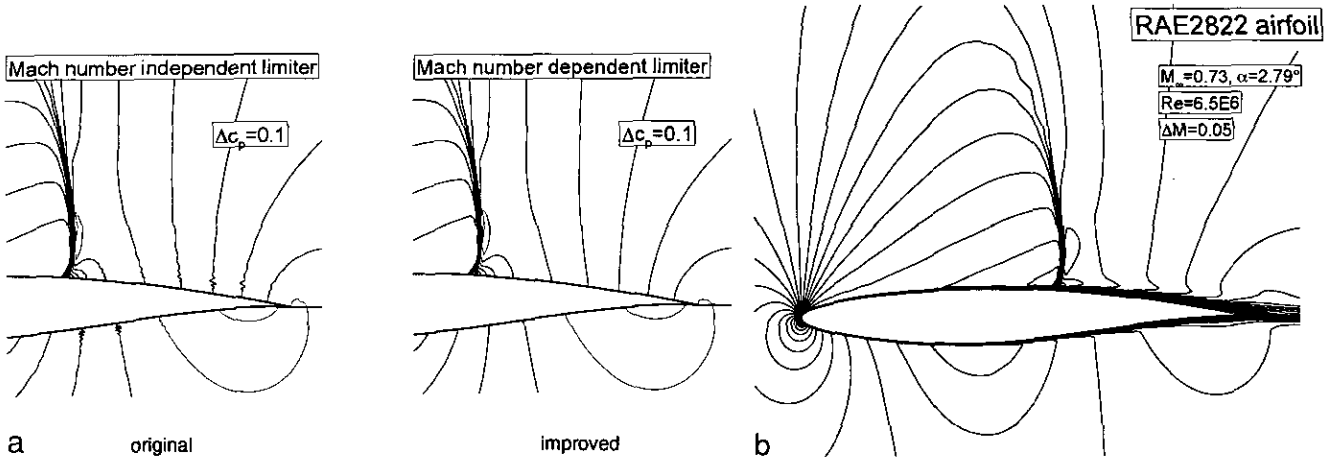

FIG. 2. Flow solution for RAE 2822 airfoil, $M_\infty = 0.73$, $\alpha = 2.79°$, $Re = 6.5 \times 10^6$: (a) Pressure contours for original and improved AUSM; (b) Mach contours.

vicinity of shocks. Moreover, in order to improve the damping behavior of the original AUSM ($\tilde{\delta} = 0$) in regions with adverse grid and flow alignment situations, its dissipative term has been modified. As it can be seen in Eq. (22), controlled dissipation is locally introduced for small advection Mach numbers, preventing the dissipative term from approaching zero as the Mach number tends to zero. In Fig. 1 the dissipative term ϕ is plotted as a function of the Mach number. Note, that for simplicity $M_L \sim M_R$ is assumed, which is valid at least in the vicinity of $M = 0$ on a sufficiently fine computational grid.

3.2. *Scaling of the Adaptive Dissipation for Viscous Flows*

Accurate and efficient calculations of viscous flows require computational grids with high-aspect ratio cells. Therefore, the dissipation term of the improved AUSM for small advection Mach numbers (Eq. (20)) has to be properly scaled in order to avoid smearing of the shear layers in the wall-normal direction. This is realized by defining the parameter $\tilde{\delta}$ in Eq. (22), not as a constant, but as a function of the wave speeds in the individual coordinate directions,

$$\tilde{\delta}_{i+1/2,j,k} = \delta \cdot \beta_{i+1/2,j,k}, \tag{24}$$

where δ is a small constant, $0 \le \delta \le 0.5$, and β is a scaling function.

One possibility for the scaling of the adaptive dissipation is

$$\beta_{i+1/2,j,k} = \min\left\{ \max\left[\frac{|\lambda_J|}{|\lambda_I|}, \frac{|\lambda_K|}{|\lambda_I|} \right], 1 \right\}, \tag{25}$$

where λ_I, λ_J, λ_K are the spectral radii of the inviscid flux Jacobians in the i-, j-, k-coordinate directions, respectively. The quantity λ_I is defined as

$$\lambda_I = \mathbf{q} \cdot \mathbf{S}_I + c|\mathbf{S}_I|, \tag{26}$$

where $\mathbf{q} = [u, v, w]^T$ is the vector of cartesian velocities and c is the speed of sound, and $|\mathbf{S}_I|$ represents the surface area associated with the i-direction of the body-fitted coordinate system. The quantities $\lambda_J \lambda_k$ are given accordingly. The scaling functions β in the j- and k-directions are defined in a similar way. With this scaling, controlled adaptive dissipation can be introduced, which on the one hand improves the damping behavior of AUSM in adverse grid situations, but on the other hand does not degrade the accuracy of the method for grid-aligned shear layers. Additional dissipation as a function of the grid aspect ratio is fed in only along the long sides of the cell, that is, if the cell face area $|\mathbf{S}_I|$ is smaller than the areas $|\mathbf{S}_J|$ and $|\mathbf{S}_K|$. On the contrary, if the cell face area $|\mathbf{S}_I|$ is larger than areas $|\mathbf{S}_J|$ and $|\mathbf{S}_K|$, as is typical in the wall-normal direction, the original nonsmearing dissipation of the AUSM is recovered.

3.3. *High-Order Scheme*

The spatial accuracy of the improved flux vector split scheme depends on the determination of the left and right states at the cell interfaces. For a first-order scheme the flow quantities at the left and right states are given by their values at the neighboring mesh points, i.e., i, j, k and $i + 1$, j, k, respectively. Higher order accuracy is obtained with the MUSCL approach in the present work. MUSCL uses extrapolation of flow quantities for the calculation of the left and right states. With this approach several decisions must be taken which affect the ability of the scheme to capture strong shocks and viscous shear layers aligned with the coordinate grids. These are the choice

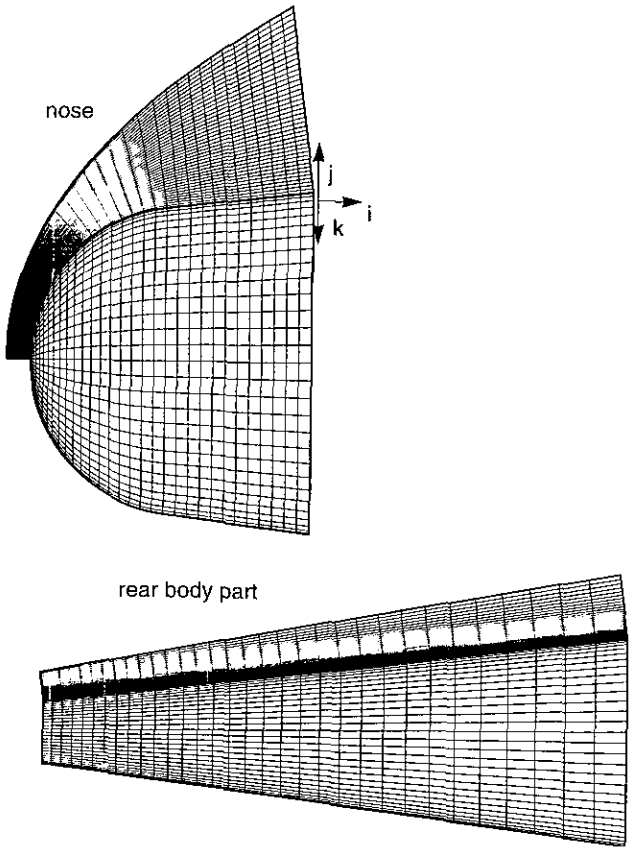

FIG. 3. Grid around blunt slender cone with spherical nose shape.

of the flow variables to be extrapolated to the cell face and the choice of the extrapolation function which gives higher order fluxes in smooth regions of the flow. At discontinuities the function switches to first-order accuracy in order to guarantee shock capturing without spurious oscillation. Here, the van Albada limiter function is chosen according to [16]

$$u_{i_L} = u_{i,j,k} + \frac{1}{2}\frac{(\Delta_+^2 + \varepsilon)\,\Delta_- + (\Delta_-^2 + \varepsilon)\,\Delta_+}{\Delta_+^2 + \Delta_-^2 + 2\varepsilon} \tag{27}$$

with

$$\Delta_+ = u_{i+1,j,k} - u_{i,j,k}$$

$$\Delta_- = u_{i,j,k} - u_{i-1,j,k},$$

where u_L denotes the flow quantity u to be extrapolated to the face $i + \frac{1}{2}$. The right state, u_R, is evaluated similarly by using the data of points (i, j, k), $(i + 1, j, k)$, $(i + 2, j, k)$. This limiter function is equivalent to Fromm's scheme in smooth regions of the flow where the gradients squared, Δ_+^2, Δ_-^2, are small compared to ε. In [16] the quantity ε is used in order to suppress limiting of the solution in regions where the flow is near constant. This is accomplished by taking

$$\varepsilon = \kappa_1\,\Delta x^n \tag{28}$$

where Δx denotes the distance between the grid points (i, j, k) and $(i + 1, j, k)$. κ_1 is an empirical constant of $O(10)$ and $2 < n < 3$. Note that one can only expect Eq. (28) to work well when solving the flow equations in their nondimensional form. Equation (28) can be extended to suppress limiting the fluxes within boundary layers. Not only does limiting in the wall-normal direction degrade accuracy on coarse meshes but it may also introduce spurious oscillations in the solution as seen in Fig. 2a. Here, we encounter the situation that the cartesian velocity components, u and v, are nonzero but the contravariant velocity component in the wall-normal direction is close to zero. Limiting the extrapolation of u and v individually, as is standard practice in most MUSCL implementations [17], may result in false values for M_L and M_R which define the inherent dissipation of the split flux (13). This problem is resolved by defining

$$\varepsilon = \max[(\kappa_1\,\Delta x^n),\ \kappa_2(\Phi_{i+1/2,j,k}^{\text{modAUSM}} - \overline{M})], \tag{29}$$

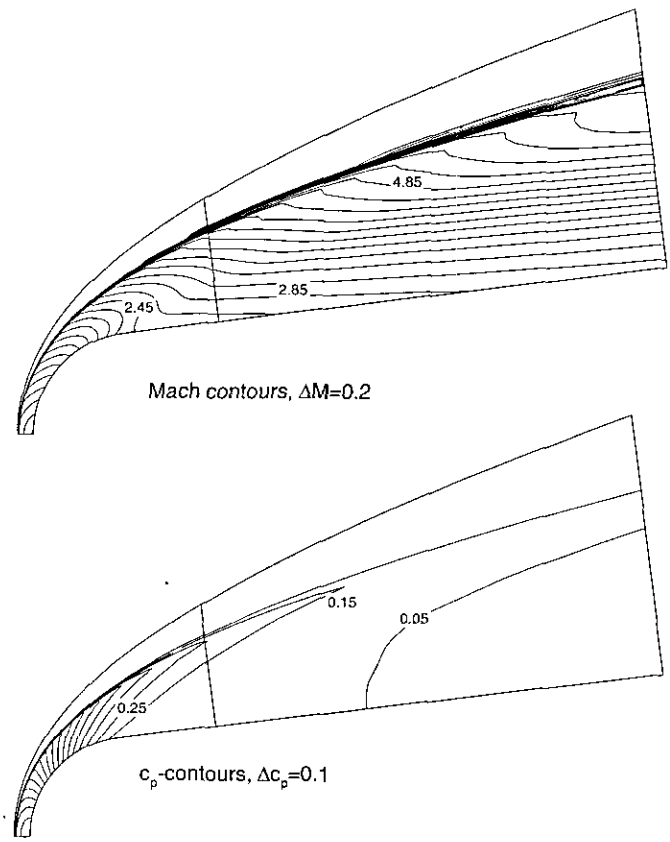

FIG. 4. Mach contours and pressure contours for blunt cone, $M_\infty = 8$, $\alpha = 0°$.

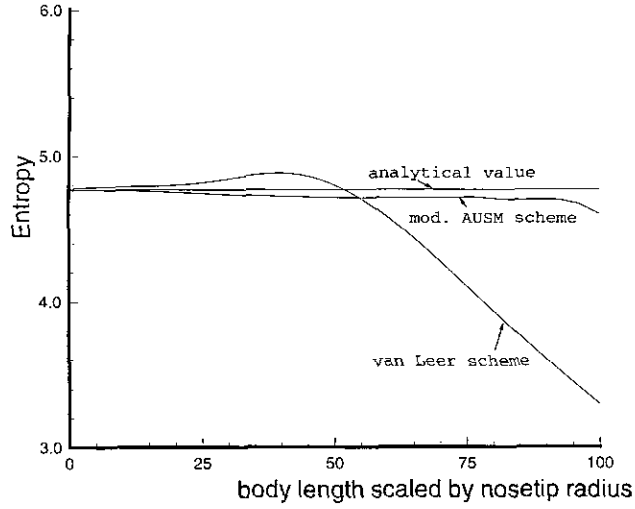

FIG. 5. Entropy value along the body, blunt cone at $M_\infty = 8$, $\alpha = 0°$.

where $\kappa_2 = O(100)$, Φ^{modAUSM} is evaluated according to Eq. (22) with $\tilde{\delta} = O(0.1)$, and $\overline{M}$ is the average of the contravariant Mach numbers at points (i, j, k) and $(i + 1, j, k)$. Figure 2a demonstrates that oscillations in the wall-normal direction are completely removed by using Eq. (29), instead of (28). Note that this type of oscillation does not occur in the higher order results published in [6]. This may be explained by the fact that the viscous test cases selected by [6] used cartesian meshes, where the cartesian velocity v is equal to the corresponding contravariant velocity component. For this special case Eq. (28) is sufficient in order to obtain proper dissipative terms.

It should also be mentioned that the second-order interpolant in Eq. (27) may be replaced by the third-order formula of [18]. This alternative yields somewhat more accurate results

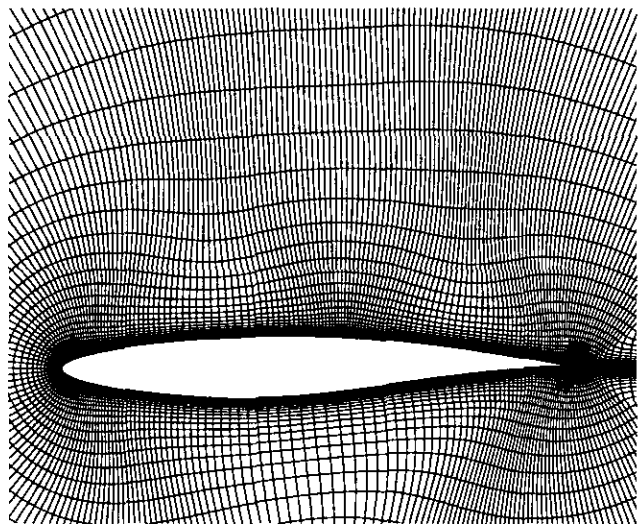

FIG. 6. Coordinate mesh for RAE 2822 airfoil with 320 × 64 cells.

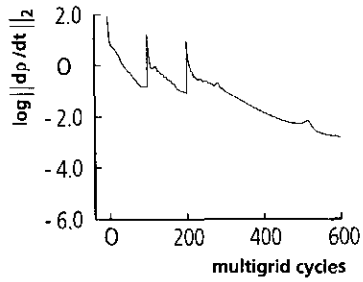

FIG. 7. Convergence history for AUSM, RAE 2822 airfoil, $M_\infty = 0.73$, $\alpha = 2.79°$, $Re = 6.5 \times 10^6$.

for transonic and supersonic flows, but it is less robust for hypersonic flows with strong shocks.

The selection of flow variables for the extrapolation process is described next. Initially, we tried some standard choices; these are the use of primitive or conserved flow variables for extrapolation. It turned out that the latter choice is not robust at transient shock waves, whereas the former tends to support oscillations in stagnation point regions behind strong shocks. Furthermore, either choice does not allow inviscid steady-state solutions with constant total enthalpy.

Constant total enthalpy in the steady state can be obtained if the energy flux in Eq. (13) is formed with total enthalpy H being an extrapolated quantity. However, recalculation of the pressure p in Eq. (13) from a single set of flow variables including H does not yield nonoscillatory fluxes for the momentum equation. Further numerical experiments showed that extrapolation of the primitives for mass and momentum fluxes, combined with extrapolation of H in order to compute the energy flux, results in nonoscillatory flow solutions and superior convergence behavior. This numerical tratment corresponds closely to the underlying design principle of the AUSM, which splits the flux vector into an advective part and a pressure part. We note that the present treatment of extrapolation for the energy equation is similar to current practice in central difference schemes [19].

In the computations of 3D hypersonic flow problems presented here, very strong shocks occurred in regions of strong variations of the grid metrics. For these cases shock resolution is further improved by modifying the limiter function, Eq. (27), as

$$u_L = u_{i,j,k} + \frac{1}{2}\nu_{i,j,k}\frac{(\Delta^{2+} + \varepsilon)\Delta_- + (\Delta^{2-} + \varepsilon)\Delta_+}{\Delta_+^2 + \Delta_-^2 + 2\varepsilon} \tag{30}$$

with pressure switch ν given by Eq. (23). Additionally, the contravariant Mach numbers, M_L and M_R are obtained by extrapolation of the contravariant velocity component. More specifically, M_L at cell face $i + \frac{1}{2}$ is computed by taking

$$M_L = \frac{(q_n)_L}{c_L}, \tag{31}$$

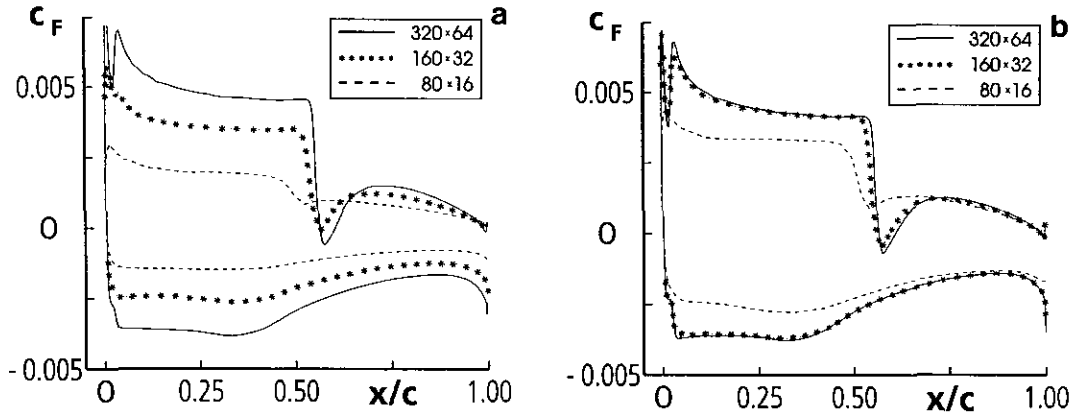

FIG. 8. Distributions of skin friction along RAE 2822 airfoil, $M_\infty = 0.73$, $\alpha = 2.79°$, $Re = 6.5 \times 10^6$: (a) van Leer flux vector splitting; (b) improved AUSM.

where $(q_n)_L$ is the contravariant velocity which is evaluated with the help of Eq. (30) and

$$(q_n)_{i,j,k} = \frac{\mathbf{S}_{i+1/2,j,k} \cdot \mathbf{q}_{i,j,k}}{|\mathbf{S}|_{i+1/2,j,k}}$$

$$\Delta_+ = (\mathbf{q}_{i+1,j,k} - \mathbf{q}_{i,j,k}) \frac{\mathbf{S}_{i+1/2,j,k}}{|\mathbf{S}|_{i+1/2,j,k}}$$

$$\Delta_- = (\mathbf{q}_{i,j,k} - \mathbf{q}_{i-1,j,k}) \frac{\mathbf{S}_{i-1/2,j,k}}{|\mathbf{S}|_{i-1/2,j,k}}$$

and c_L denotes the speed of sound associated with the left state.

3.4. *Time Integration*

The spatial discretization results in a system of ordinary differential equations with respect to time. For the inviscid blunt cone calculation the solution has been advanced in time employing an explicit five-stage scheme. Local time stepping and implicit residual damping have been applied to accelerate the convergence to the steady state. Furthermore, a space marching technique has been used which considerably reduces the overall computational expense [20]. The viscous flow problems were computed using multigrid techniques coupled with either explicit multistage time stepping [13] or the implicit LU-SSOR scheme [21].

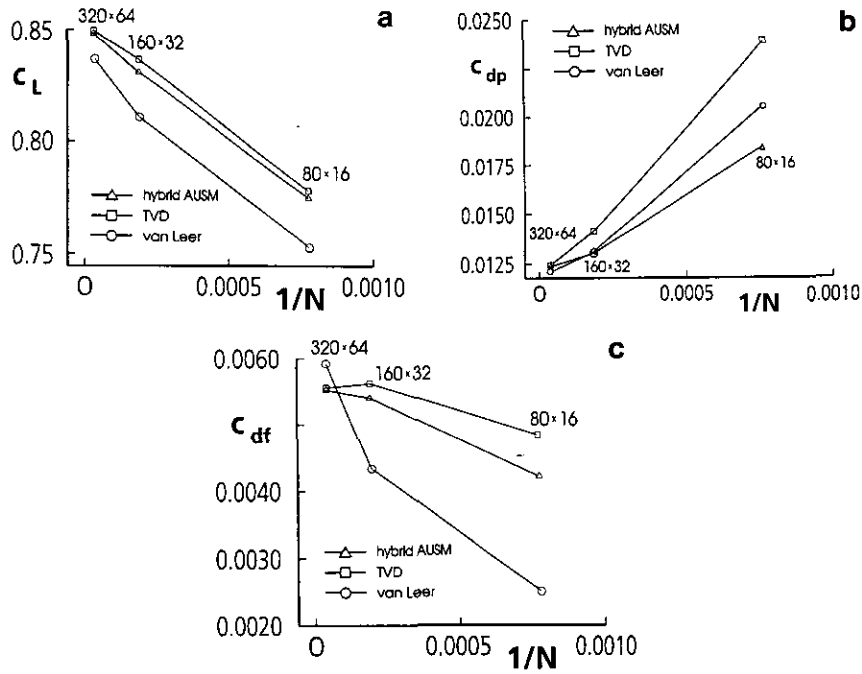

FIG. 9. Grid convergence of force coefficients for RAE 2822 airfoil, $M_\infty = 0.73$, $\alpha = 2.79°$, $Re = 6.5 \times 10^6$: (a) lift coefficient; (b) pressure drag; (c) friction drag.

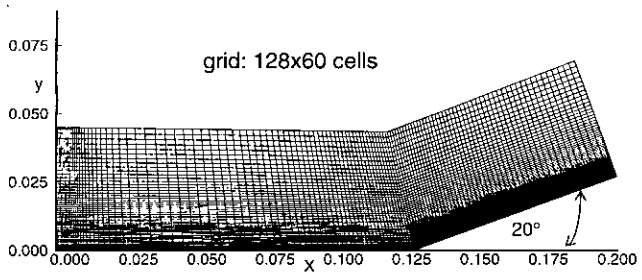

FIG. 10. Grid for 20° compression ramp.

4. NUMERICAL RESULTS

In the following, numerical results for inviscid and viscous flows obtained with the improved advection upstream splitting method are presented. Emphasis is put on the method's capability to resolve the wall-normal gradients of flow quantities which, for instance, occur in entropy and boundary layers. As test cases the inviscid flow around a blunt slender cone and viscous 2D and 3D flows are selected.

4.1. *Inviscid Flow around a Blunt Cone*

Inviscid calculations around a blunt slender cone [22] at freestream Mach number $M_\infty = 8$ and angle of attack $\alpha = 0°$ have been carried out. The curved bow shock detached from the blunt nose produces a thick entropy layer in the front part of the configuration which, however, develops to a very thin layer in the rear part. Since the quality of the numerical results strongly depends on the resolution of the entropy layer, computational methods have to be used which accurately predict this flow feature.

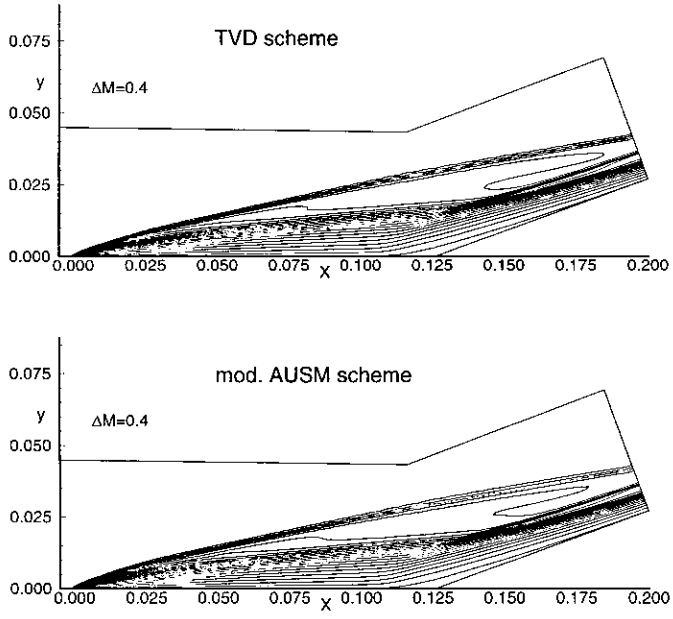

FIG. 11. Mach contours for 20° compression ramp, $M_\infty = 10$, $Re_c = 18119$.

The grid used for the calculations is shown in Fig. 3. The C-O topology has been chosen with $161 \times 41 \times 31$ grid points in i-, j-, k-directions, respectively; 21 grid points were used to discretize the spherical nose shape in streamwise direction. In i- and j-directions a linear stretching of the grid spacing was introduced. This allows a suitable grid distribution with respect to computational efficiency. The stretching in j-direction provides grid points in the near-wall region in order to resolve the thin entropy layer in the rear part of the configuration.

Figure 4 shows Mach number and pressure contours in the nose region obtained with the improved flux splitting method. The flow field is axi-symmetric since the angle of attack has been set to zero. In order to check the accuracy of the scheme; in Fig. 5 the entropy value at the wall is plotted along the body in streamwise direction. Since for inviscid flows the body surface is part of the stagnation streamline, the entropy is constant along the body. Its value is determined through the entropy rise across the normal shock. In Fig. 5 numerical results obtained with the improved AUSM and with the classical van Leer scheme are depicted. In addition, the analytical entropy value at the wall is given. In the front part of the configuration (almost up to 100 nose radii) the error of AUSM is less than 1%. In the rear part, however, the accuracy is decreasing. This may be attributed to the computational grid, which in this part of the configuration is not sufficiently fine to resolve the thin entropy layer as accurately as in the front part. It should be noted that $\delta = 0.1$ has been used to control the dissipative term. Computations with different parameters for δ did not improve the results. As can be seen in Fig. 5, the classical van Leer scheme produces less accurate results along the whole configuration. This demonstrates that on a given grid the improved flux splitting method is less diffusive compared to the van Leer scheme and, therefore, it is better qualified for the accurate resolution of entropy layers.

4.2. *Viscous 2D Flows*

Two-dimensional viscous flow problems serve to demonstrate the ability of the new flux vector split scheme to resolve viscous shear layers. We have chosen transonic and hypersonic test cases which are well known from literature.

The first test case is the transonic turbulent flow over the RAE 2822 airfoil. The onflow conditions correspond to CASE 9 of [23]. The computational grid consists of 320×64 cells. Grid points are clustered around the leading edge and trailing edge, as well as in the shock region at the upper surface; see Fig. 6. Flow computations were carried out with explicit multistage time stepping and multigrid with full coarsening. A typical convergence history is displayed in Fig. 7. Computing time was reduced by a full multigrid; that is, coarse-mesh solutions on grids with 80×16 cells and 160×32 cells were obtained with each 100 multigrid iterations in order to produce

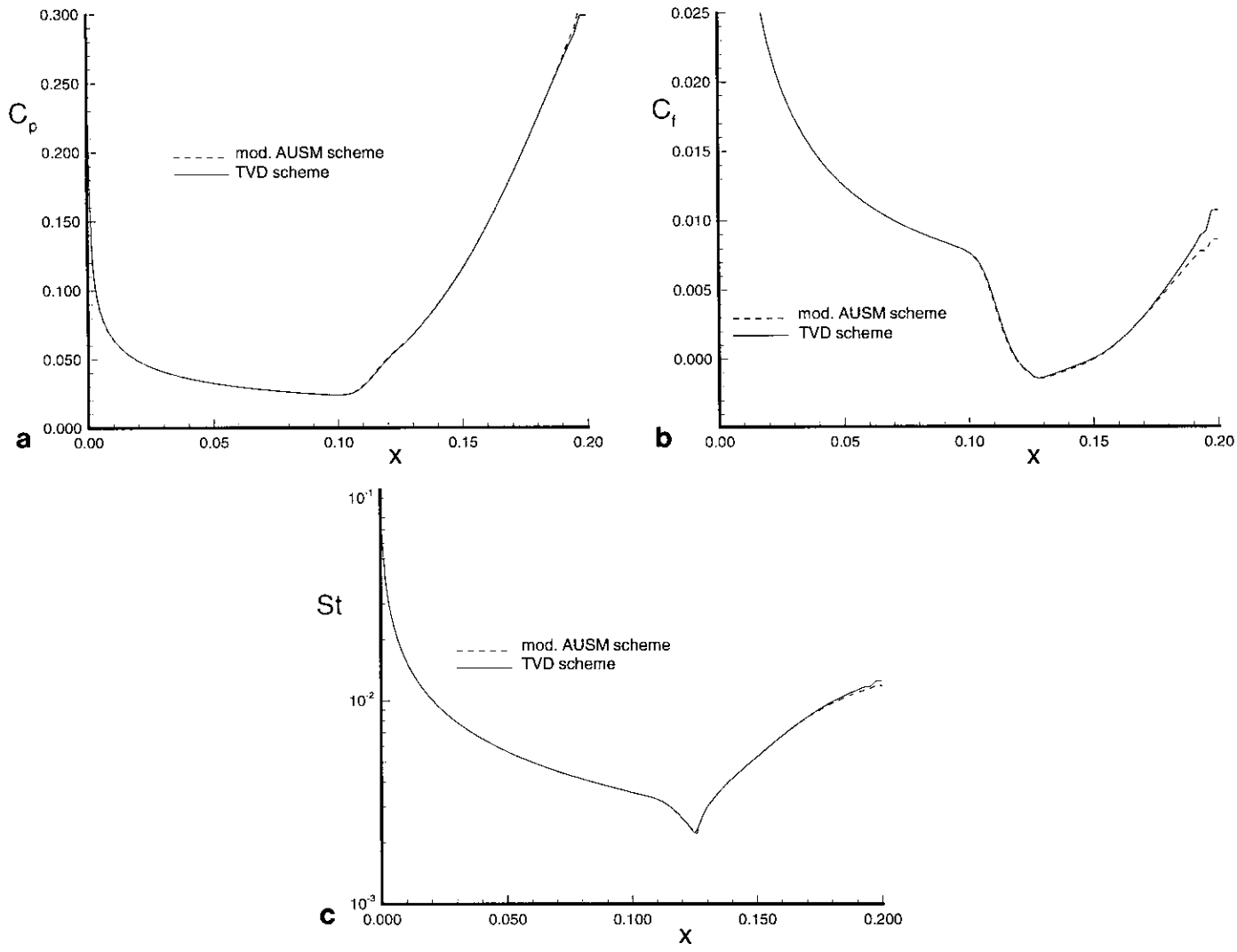

FIG. 12. Flow solution for 20° compression ramp, $M^* = 10$, $Re_c = 18119$: (a) pressure coefficient; (b) skin friction coefficient; (c) Stanton number.

the initial solution on the next finer grid. An impression of the overall flow field is provided by Fig. 2b. The improved AUSM yields a clean resolution of the shock and the boundary layers. Figure 8 compares the distributions of skin friction yielded by the AUSM and van Leer schemes under grid refinement. There is a dramatic improvement of resolution visible for the improved AUSM. Not only does the improved resolution of shear layers affect the friction drag of the airfoil, but also the pressure forces, due to viscous/inviscid interaction. This is demonstrated in Fig. 9, where lift and drag values are plotted as a function of the inverse of the total number of cells, N. The results of an alternative high resolution scheme based on flux difference splitting [24, 25] are included for comparison. The smeared boundary layers of van Leer's scheme affect the interaction with the shock in that the shock location moves upstream (not shown here). Consequently, lift is underpredicted by van Leer's scheme as compared to the AUSM and upwind TVD. The improved AUSM is best for the prediction of pressure drag, whereas the AUSM and upwind TVD do similarly well for skin friction drag.

The next test case presented is the hypersonic laminar flow past a 20° compression ramp. The onflow conditions correspond to the case III.2 of the *Workshop on Hypersonic Flows for Reentry Problems, Antibes, 1991* [26]. These computations were carried out with the implicit LU-SSOR scheme and multigrid [21]. Note that some reference computations with explicit time stepping yielded the same steady-state solutions. An interpolated coarse mesh result served as initial solution for the computations. The computational grid plotted in Fig. 10 consists of 128 × 80 cells. The onflow conditions are $M_\infty = 10$, $Re_c = 18119$, $T_\infty = 52$ K, and $T_w/T_\infty = 5.57$ (constant wall temperature). Figure 11 shows the computed Mach contours. Results obtained with the upwind TVD scheme [24, 25] and the modified AUSM with the parameter $\delta = 0.05$ are

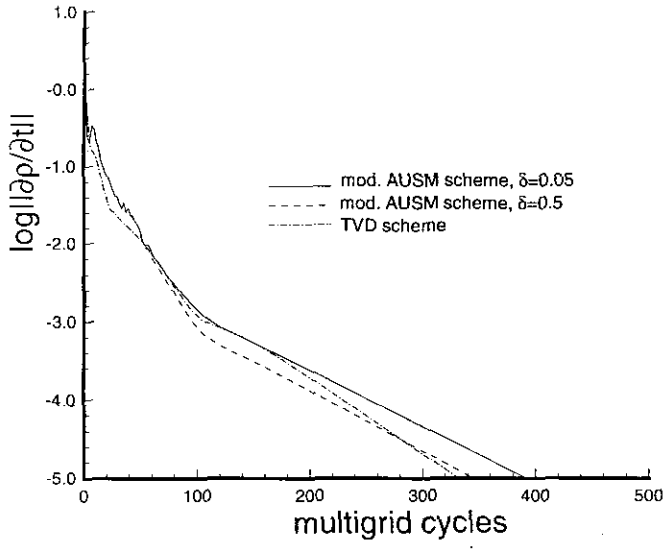

FIG. 13. Convergence history for 20° compression ramp, $M_\infty = 10$, $Re_c = 18119$, influence of parameter δ with scaling function Eq. (25).

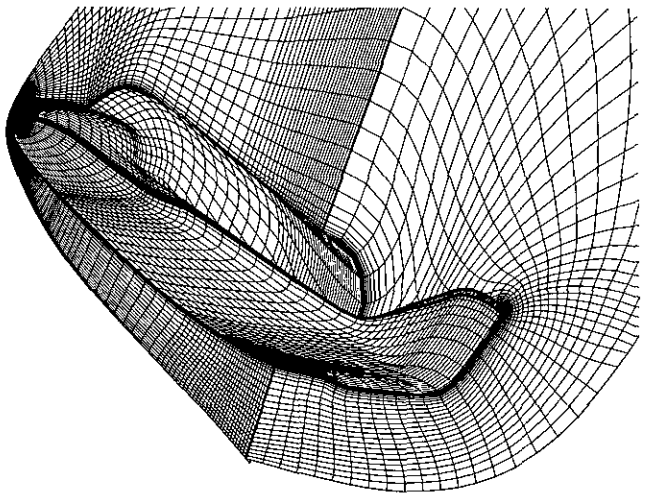

FIG. 15. Discretized HERMES reentry vehicle with 72 × 48 × 32 cells, surface grid, plane of symmetry, and outflow grid plane.

shown. The pressure coefficient, the skin friction coefficient, and the Stanton number along the wall are displayed in Figs. 12a–c. No major differences can be observed between the schemes. Only in the skin friction plot there is a noteworthy deviation in the last 10% of the configuration. Here the improved AUSM predicts a smaller skin friction value. Note that the results agree very well with the grid-converged solutions published in [25]. Figure 13 presents a comparison of the convergence histories between the TVD scheme and the improved AUSM. The fastest convergence is obtained with the TVD scheme. The modified AUSM shows a slower asymptotic convergence behavior which is independent of the parameter δ. There is no influence of the dissipation parameter δ on the skin friction (not shown here). In Figs. 14a–b a comparison of the first- and second-order results obtained with the TVD scheme and the improved AUSM with $\delta = 0.05$ is presented. For both schemes the asymptotic convergence behavior (Fig. 14a) is worse for the second-order calculation compared to the first-order one. It is interesting to note, that also in the first-order mode, without any extrapolation procedures for second-order accuracy and without any limiter functions, the flux difference split scheme shows a better convergence rate than the modified

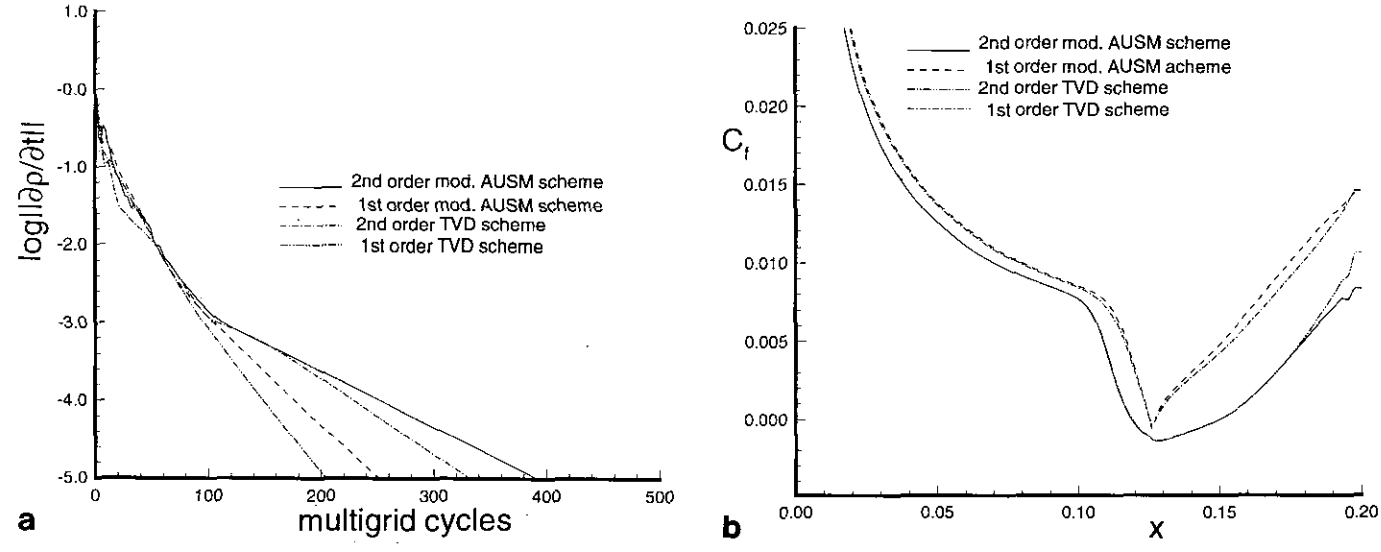

FIG. 14. Effect of spatial discretization schemes on convergence and accuracy of solution for 20° compression ramp, $M_\infty = 10$, $Re_c = 18119$: (a) convergence history; (b) skin friction coefficient.

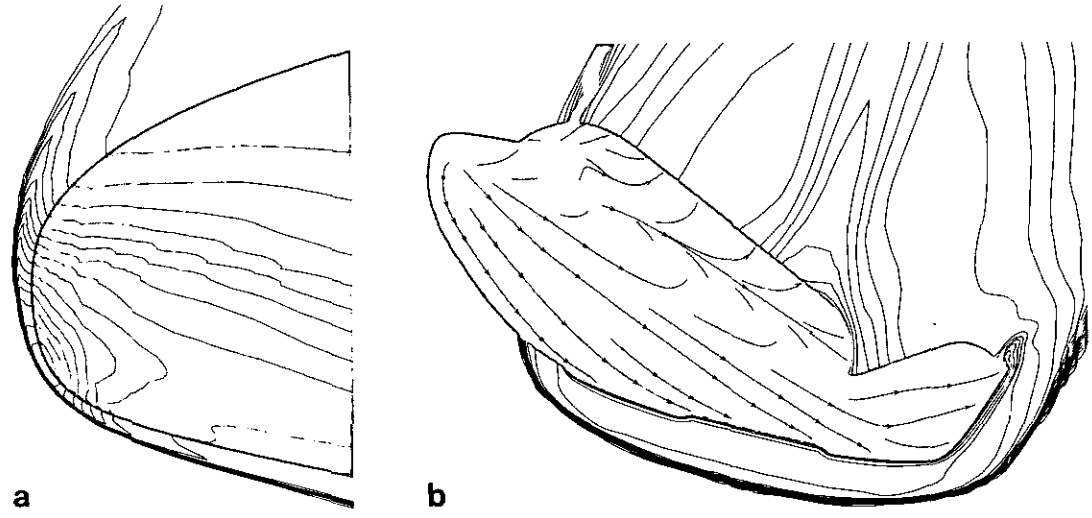

FIG. 16. Computed flow field around HERMES reentry vehicle at $M_\infty = 25$, $\alpha = 30°$, $H = 75$ km for air in thermochemical equilibrium: (a) pressure contours in plane of symmetry near the nose; (b) surface streamlines and Mach contours in outflow plane.

AUSM. This indicates better damping properties of the flux difference splitting. One may recall that the AUSM scales the dissipation with the local Mach numbers in contravariant directions, whereas the flux difference split approach scales the dissipation with the individual speed of the acoustic and convective waves [3]. Comparison of the skin friction along the wall (Fig. 14b) illustrates the difference between the first- and the second-order results. Both schemes show the same behavior.

4.3. *Three-Dimensional Hypersonic Viscous Flow*

The final numerical test case is the 3D viscous flow over the reentry vehicle HERMES. This case will demonstrate that the present discretization method is useful for 3D flows around complex geometries including strong shocks and strong flow expansions into leeside flow regions. Figure 15 displays the surface grid of the configuration and some selected planes of the field grid. Here, every second grid point was plotted for clarity. The complete 3D grid wraps around the vehicle with a C-O topology and contains 145×97 surface points and 65 points in the wall-normal direction. Note that a polar singularity forms at the nose of the vehicle.

Freestream flow conditions were chosen as $M_\infty = 25$ and $\alpha = 30°$. For this case, air was assumed to be in thermochemical equilibrium, and the freestream values of density and internal energy correspond to an altitude of 75 km. A converged flow solution for the complete flow field took about 300 iterations of the multigrid algorithm with explicit multistage time stepping. Figure 16a displays the captured bow shock in the nose region of the vehicle. Figure 16b shows the wall stream lines and Mach number contours in the outflow plane. At these flow conditions the bow shock is very close to the vehicle. High-pressure flow occurs along the lower windward surface of the configuration and produces almost all of the lift. A strong flow expansion takes place around the leading edges of the wing and the winglet into the leeside with low pressure and density. Note, that this flow situation could not be computed with the upwind TVD scheme, presumably, because this scheme does not preserve the total enthalpy in the steady state. Grid refinement investigations (not shown here) indicate that the numerical errors of the predicted heat transfer distributions are smaller than 10%. Since then, the improved AUSM was successfully applied to other complex hypersonic flow problems, including deflected control surfaces [27] and multiblock computations of the flow through the slot between different control surfaces [28].

5. CONCLUSIONS

A new flux vector splitting scheme has been investigated for accurate and efficient prediction of hypersonic flows. This scheme is based on the advection upstream splitting method (AUSM) recently developed by Liou and Steffen. It is characterized by its low numerical diffusion and its low computational costs.

AUSM in its original form produces pressure oscillations near strong shocks and in adverse grid situations. In order to improve the shock resolution capability and the damping behavior of AUSM, a hybrid method is proposed which switches from the AUSM flux to the classical van Leer flux at shock waves, thus ensuring a clean and sharp shock resolution. Furthermore, an adaptive dissipative term is introduced which prevents the scheme to be undamped as the cell face Mach number approaches zero. This provides sufficient numerical damping in cases of adverse grid situation and flow alignment. The hybrid flux vector split scheme is cast in a form which characterizes its behavior at low Mach numbers very well.

The improved AUSM is investigated with respect to the computation of entropy and boundary layers. In order to avoid numerical smearing, scaling functions are introduced, which properly scale the adaptive dissipative term on computational grids with high aspect ratio cells necessary for efficient resolution of entropy and boundary layers. The calculation of the axisymmetric inviscid flow around a blunt slender cone shows that the modified AUSM with proper scaling of the dissipative term is capable of accurate entropy layer predictions. Furthermore, the calculations for 2D airfoils and 2D ramp flows demonstrate that the proposed method predicts viscous flows as accurate as the TVD flux difference splitting scheme. Compared to the TVD scheme the convergence behavior of the modified AUSM scheme is slightly worse. However, due to the reduced computational effort per time step, the overall efficiency of both methods is comparable. Since in contrast to the TVD scheme the numerical effort of AUSM is proportional to the number of unknowns, relative reduction of the computational cost is obtained for 3D calculations and also for solutions of flow problems with additional conservation equations. Computations of a complex 3D viscous flow over a winged reentry vehicle demonstrate the usefulness of the present discretization for general 3D applications. The AUSM enabled us to compute flows with very strong shocks and strong expansions into leeside flow regions, which were impossible with flux difference splitting.

ACKNOWLEDGMENTS

The authors thank J. Stilla for providing the computational grid of the blunt cone test case and J. Blazek, who gave us the 2D implicit code used for the hypersonic ramps.

REFERENCES

1. J. L. Steger and R. F. Warming, *J. Comput. Phys.* **40,** 263 (1981).
2. B. Van Leer, "Flux-Vector Splitting for the Euler Equations," in *Lecture Notes in Physics*, Vol. 170 (Springer-Verlag, New York/Berlin, 1982), p. 507.
3. P. L. Roe, *J. Comput. Phys.* **43,** 357 (1981).
4. H. C. Yee and A. Harten, *AIAA J.* **25,** 266 (1987).
5. D. Hänel and R. Schwane, AIAA Paper 89-0274 (unpublished).
6. M.-S. Liou and Ch. Steffen, *J. Comput. Phys.* 107(1), 23 (1993).
7. F. Coquel and M.-S. Liou, "Stable and Low Diffusive Hybrid Upwind Splitting Methods," in *Proceedings, 1st European CFD Conference, Brussels, 1992* (unpublished).
8. M.-S. Liou, "On a New Class of Flux Splittings," in *Lecture Notes in Physics*, Vol. 414 (Springer Verlag, New York/Berlin, 1992), p. 115.
9. L. Bergamini and P. Cinnella, AIAA-93-0876 (unpublished).
10. J. Grönner, M. Hilgenstod, and E. von Lavante, Univeristät-GH-Essen, 45/27 Essen, August 1993 (unpublished).
11. B. S. Baldwin and H. Lomax, AIAA 78-257 (unpublished).
12. Ch. Mundt, R. Keraus, and J. Fischer, *Zeitschrift Flugwissendraft und Weltraumtorschung* **15,** 179 (1991).
13. R. Radespiel, C.-C. Rossow, and R. C. Swanson, *AIAA J.* 28(8) (1990).
14. E. Turkel, *Appl. Numer. Math.* **12,** 257 (1993).
15. A. G. Godfre, R. W. Walters, and B. Van Leer, AIAA 93-0535 (unpublished).
16. V. Ventkatakrishnan, AIAA 93-0880 (unpublished).
17. B. Van Leer, "Upwind Difference Methods for Aerodynamics Governed by the Euler Equations," in *Lectures in Applied Mathematics*, Vol. 22, edited by B. Engmist, S. Osher, and R. Sommerville (Amer. Math. Soc., Providence, RI 1985), Part II, p. 327.
18. S. L. Krist, J. L. Thomas, W. L. Sellers, and S. O. Kjelgaard, AIAA 90-0429 (unpublished).
19. A. Jameson, W. Schmid, and E. Turkel, AIAA 81-1259 (unpublished).
20. J. Schöne, N. Kroll, and Th. Streit, "Steps towards an Efficient and Accurate Method Solving the Euler Equations around a Reentry Configuration at Supersonic and Hypersonic Speeds," in *Proceedings, European Symposium on Hypersonics, ESTEC, ESA SP-318, 1991*, p. 115.
21. J. Blazek, AIAA 94-0062 (unpublished).
22. K. F. Stetson, E. R. Thompson, J. C. Donaldson, and L. G. Siler, AIAA 84-0006 (unpublished).
23. P. H. Cook, M. A. McDonald, and M. C. P. Firmin, AGARD Advisory Rept. 138, May 1979.
24. N. Kroll and C.-C. Rossow, "A High Resolution Cell Vertex TVD Scheme for the Solution of the Two- and Three-Dimensional Euler Equations," in *Lecture Notes in Physics*, Vol. 371 (Springer-Verlag, New York/Berlin, 1990), p. 442.
25. R. Radespiel and R. C. Swanson, *J. Comput. Phys.* **116**(1) 103 (1995).
26. R. Abgrall *et al.* (Eds.), *Hypersonic Flows for Reentry*, Vol. III (Springer-Verlag, Berlin/Heidelberg, 1992).
27. J. M. A. Longo and R. Radespiel, "Flap Efficiency versus Flap Heating for a Winged Reentry Vehicle—A Challenge for the CFD, in *Proceedings, 19th ICAS Congress, Anaheim, CA, Sept. 18–24, 1994*; Paper 94-5.2.1.
28. U. Herrmann, R. Radespiel, and J. M. A. Longo, AIAA 94-0629 (unpublished).